

SYNTHESIS, CHARACTERIZATION AND ELECTROCHEMICAL PERFORMANCE OF ACTIVATED CARBON SUPPORTED MnO₂ FOR ELECTROCHEMICAL CAPACITOR

Luong Thi Thu Thuy, Le Van Khu, Nguyen Thi Kim Lien

Faculty of Chemistry, Hanoi National University of Education, 136 Xuan Thuy St.,
Cau Giay Dist., Ha Noi

*Email: thuyltt@hnue.edu.vn

Received: 20 December 2017; Accepted for publication: 1 September 2018

Abstract. MnO₂ was synthesized by adding activated carbon into KMnO₄ solution and stirred in a magnetic or ultrasonic stirrer. The obtained MnAC samples were characterized by means of XRD, TGA, TPR-H₂, SEM and BET. All samples are amorphous and have porous structure. MnAC-M prepared by magnetic stirring have higher manganese content, earlier reduction temperature, smoother surface area while MnAC-U prepared by ultrasonic stirring have larger specific surface area and pore volume. Electrochemical studies revealed that at low scan rate the specific capacitance of MnAC-U is larger than that of MnAC-M, while at high scan rate the specific capacitance of MnAC-M is higher. All the results indicated that the differences of the performances of MnAC electrodes from the different stirring methods arose from the different microstructure characteristic and the metal oxide loading of MnAC samples.

Keywords: electrochemical capacitor, activated carbon, manganese oxide, magnetic stirring, ultrasonic stirring.

Classification numbers: 2.4.4; 2.8.2

1. INTRODUCTION

Along with the development of sustainable energy which has intermitten nature, the need of energy storage system has grown dramatically in recent years. Due to the high power density, excellent reversibility and long cycle life, electrochemical capacitors have been attracting worldwide attention. Based on the charge storage mechanisms, electrochemical capacitor can be classified into two groups: i) Electric double layer capacitor (EDLC) that uses high surface area materials as electrode and store charge at the interface and ii) Pseudo-capacitors that uses fast and reversible reaction of transition metal oxides or conducting polymers for charge storage [1].

MnO₂ is one of the most inexpensive, abundant and non-toxic cathodic materials with high theoretical capacitance (1370 F g⁻¹, Mn⁴⁺ → Mn³⁺ [2]). However, the low reversibility of oxidation/reduction and the low conductivity of MnO₂ (10⁻⁵ - 10⁻⁶ S cm⁻¹ [3]) reducing its capacitance, which in turn limits its commercialization. Introducing MnO₂ onto activated carbon

surface has been proved to greatly increase the conductivity as well as the specific capacitance of the active material [4].

Chemical precipitation method is among the simplest techniques for synthesizing MnO₂ nanoparticles. However, in MnO₂/activated carbon case, MnO₂ tend to aggregate into bigger particles which in turn decrease the active sites and cause the blockage of the activated carbon pores [5]. Hence, stirring is essential to prevent the particle agglomeration/aggregation and is one of the prime issues to increase the performance of MnO₂/activated carbon materials. Particle size, specific surface area, and pore volume can vary substantially when using different stirring methods. This work presents the synthesis and characterization of MnAC materials and the effect of stirring methods, namely magnetic and ultrasonic stirring, to electrochemical property of the as-prepared materials based on cyclic voltammetry (CV) and galvanostatic charge/discharge tests.

2. MATERIALS AND METHODS

2.1. Materials

2.1.1. Synthesis of MnAC materials

Rice husk base activated carbon (RH-AC) was prepared using the mixture of NaOH and KOH as activating agents and was activated at 800 °C. Some features of RH-AC including: specific surface area 2990 m² g⁻¹, micropore surface area 2747 m² g⁻¹, external surface area 243 m² g⁻¹, micropore volume 1.4316 cm³ g⁻¹, total pore volume 1.8084 cm³ g⁻¹.

All chemicals were of analytical grade and used without further purification. RH-AC was dried at 120 °C in 5 hours and dry ball milled at 500 rpm in a Fritsch Pulverisette 7 ball mill for 15 min. Thereafter, 1.0 g milled RH-AC was dispersed into 50 mL 0.2 M KMnO₄ solution and stirred in a magnetic or ultrasonic stirrer for 60 min. The obtained precipitates were filtered and washed several times with distilled water and then dried at 120 °C in 24 hours. MnAC materials were achieved through the following reaction: $4\text{MnO}_4^- + 3\text{C} + \text{H}_2\text{O} \rightarrow 4\text{MnO}_2 + \text{CO}_3^{2-} + 2\text{HCO}_3^-$ [6]. The resulted samples were labeled as MnAC-M and MnAC-U, in which M stands for magnetic stirring and U stands for ultrasonic stirring.

2.1.2. Electrode preparation

The fabrication of working electrodes was carried out by mixing MnAC materials, polytetrafluoroethylene (PTFE) and graphite with mass ratio of 70:15:15 and dispersed in ethanol. The resulting mixture was coated onto nickel foam substrate (1 cm²) with a doctor blade, dried at 120 °C in 10 h, and pressed under 20 MPa.

2.2. Analytical methods

X-ray diffraction (XRD) patterns were obtained on a D8 Advance (Bruker) with Cu K α radiation as the X-ray source. Thermogravimetric analysis (TGA) was collected on a thermogravimetric analyzer DTG-60H (Shimadzu) with a temperature ramp of 10 °C min⁻¹. Hydrogen temperature-programed reduction (TPR-H₂) experiments were performed using an AutoChem II instrument (Micromeritics) in the temperature range 50 ~ 600 °C with a heating rate of 10 °C min⁻¹. The morphology of the samples was observed using a scanning electron

microscope JSM-6390 (Jeol). The textural properties were investigated using physical adsorption of nitrogen at 77 K on a TriStar 3000 instrument (Micromeritics); the samples were degassed at 220 °C for 7 hours prior to all measurements.

Electrochemical behavior was investigated using an Autolab PGSTAT 302N instrument in 6M KOH electrolyte solution. The electrochemical cell was a three electrode system: the as-prepared electrode as working electrode, a platinum wire as counter electrode and the saturated calomel as reference electrode. Cyclic voltammograms (CV) were conducted between -1.1 ~ -0.1 V at scan rates of 5, 10, 30, and 50 mV s⁻¹. Galvanostatic charge/discharge measurements were recorded at current densities of 0.5, 1.0, 2.0, and 3.0 A g⁻¹ within the same voltage range of CV measurements.

3. RESULTS AND DISCUSSION

3.1. Characterization

3.1.1. XRD analysis

The XRD patterns of RH-AC, MnAC-M and MnAC-U samples are shown in Fig. 1. There are no diffraction peaks implying an amorphous structure of the samples. This result matches well with literature, that synthesis temperature below 400 °C would form amorphous MnO₂ [7].

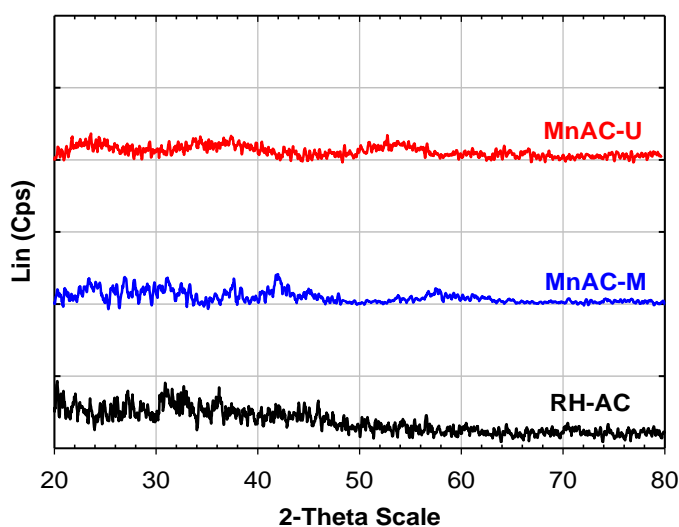


Figure 1. XRD patterns of RH-AC, MnAC-M, and MnAC-U activated at 800 °C.

3.1.2. TGA analysis

The weight loss pattern of the samples was measured by TGA and shown in Fig. 2. TGA thermogram of RH-AC is also included in Fig. 2 for comparison. For RH-AC, there are two degradation steps: i) The initial weight loss below 350 °C is ascribed the decomposition of surface functional groups (carboxyl and lactone groups); ii) The second weight loss from 350~600 °C accompanied an exothermic peak at 513.53 °C in DTA curve is attributed to the removal of more stable functional groups (phenol, carbonyl, and quinone [8]) and the degradation of the carbon skeleton [9]. For MnAC samples, the weight loss starts at about 250 °C then drastically drop in

the range of 270-300 °C and is accompanied by a sharp exothermic peak in DTA curve. This weight loss is corresponded to the removal of carbon from the sample under the catalyst of MnO₂ particles [10]. The exothermic peak of MnAC-M (271 °C) is lower than that of MnAC-U (284 °C), this apparently the effect of manganese oxide is higher in magnetic preparing sample. The weight loss in the temperature range of 300 – 400 °C is probably caused by the combustion of carbon without the presence of manganese oxide [10]. The small weight loss in the range of 400-550 °C is attributed to the loss of oxygen from MnO₂ lattice to form Mn₂O₃ [11]. RH-AC is completely combusted at 550 °C, therefore the remaining at 600 °C can be assigned to the manganese oxide (Mn₂O₃) on the activated carbon surface. The remaining of all samples and the calculated MnO₂ percentage are summarized in Table 1. It could be seen from Table 1 that the samples prepared by magnetic stirring (40.97 %) have higher manganese oxide content than prepared by ultrasonic stirring (34.25 %).

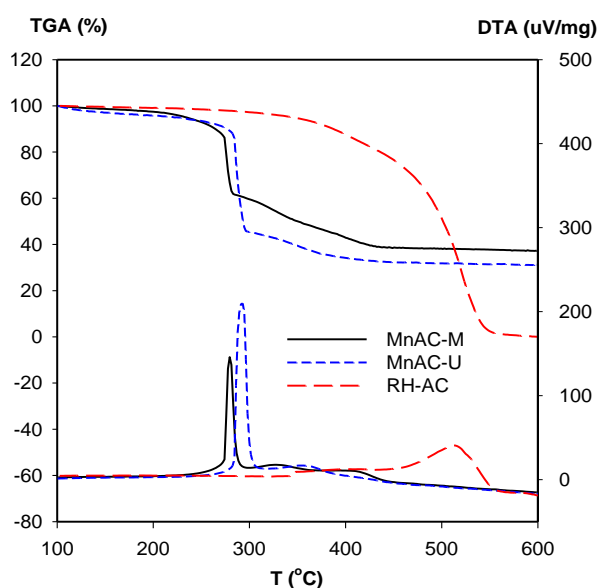


Figure 2. TGA thermograms of RH-AC and MnAC samples.

Table 1. Weight of the remaining at 600 °C and the calculated metal percentages.

Sample	% remaining weight at 600 °C	% MnO ₂
RH-AC	0.0	0.0
MnAC-M	37.2	40.97
MnAC-U	31.1	34.25

3.1.3. TPR-H₂ analysis

The TPR-H₂ characterization of MnAC samples and RH-AC are reported in Fig. 3. RH-AC is stable up to 500 °C and the small peak at 550 °C is attributed to the methanation of carbon (C + H₂ → CH₄) [12]. All the MnAC samples show three well-distinct peaks, corresponding to the reduction steps of MnO₂. The first peak at 250 °C is assigned to the reduction of MnO₂ to

Mn₂O₃. The second peak at 370 °C is the second step of reduction from Mn₂O₃ to Mn₃O₄, and the third peak at 440 °C is attributed to the reduction of Mn₃O₄ to MnO [13].

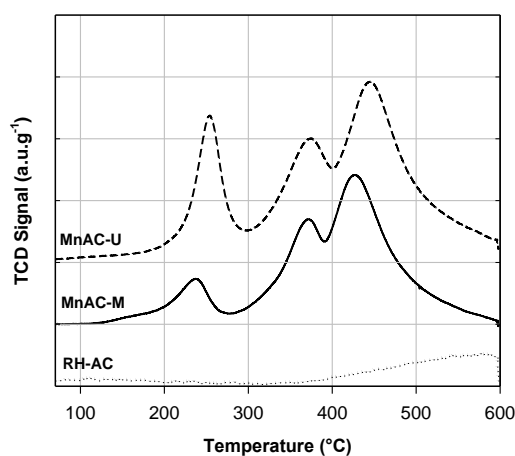


Figure 3. TPR-H₂ profile of RH-AC.

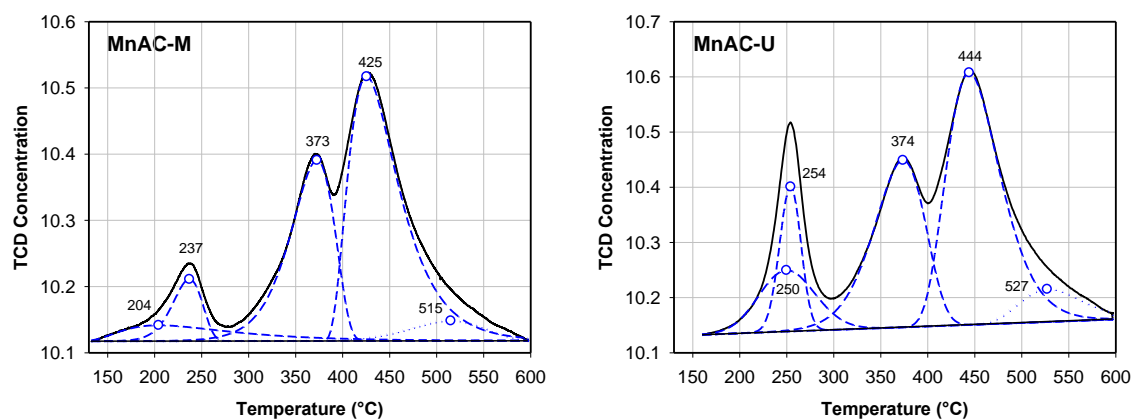


Figure 4. Deconvolution of TPR-H₂ profile of MnAC samples.

Table 2. H₂ consumption of MnAC samples.

Sample	Total H ₂ consumption (mmol g ⁻¹)	MnO ₂ (%)
MnAC-M	4.8513	42.18
MnAC-U	3.7607	32.69

It is worthy to mention that the first peak appeared earlier than the reduction temperature of α-MnO₂ or γ-MnO₂ (307~330 °C) [14], this might be because MnO₂ is in amorphous state and have good dispersion on the surface of activated carbon. Percentage of MnO₂ can be calculated after peak deconvolution (Fig. 4) with the assumption that the peak after 500 °C is the methanation of carbon and the last product is MnO (reduction sequence MnO₂ → Mn₂O₃ → Mn₃O₄ → MnO).

Total H₂ consumption and the calculated %MnO₂ are listed in Table 2. It can be seen that the manganese oxide content is higher when prepared by magnetic stirring and in good agreement with the results from TGA analysis. The variation in MnO₂ content might be explained by the different promoting effect of stirring method to the interaction between MnO₄⁻ and C as well as the removal of the products CO₃²⁻ and HCO₃⁻ out of reaction zone. The magnetic stirring might promote the interaction between MnO₄⁻ and C, which in turn increase the percentage of MnO₂ in the products compared to ultrasonic stirring.

3.1.4. SEM observation

Morphology of RH-AC and MnAC samples prepared using different stirring methods was analyzed using SEM and the images are shown in Fig. 5. RH-AC exists in the form of spherical shaped particles with diameter of 100 nm. Some of the particles are accumulated to form bigger size pieces. All MnAC samples show relatively rough morphology and bear numerous pores on the surface, which provide sufficient accessible space for electrolyte penetration. MnAC-M have small granules and more even surface, whereas MnAC-U have mixed spherical and rod-like particles with length of 400-500 nm, which caused by different stirring methods.

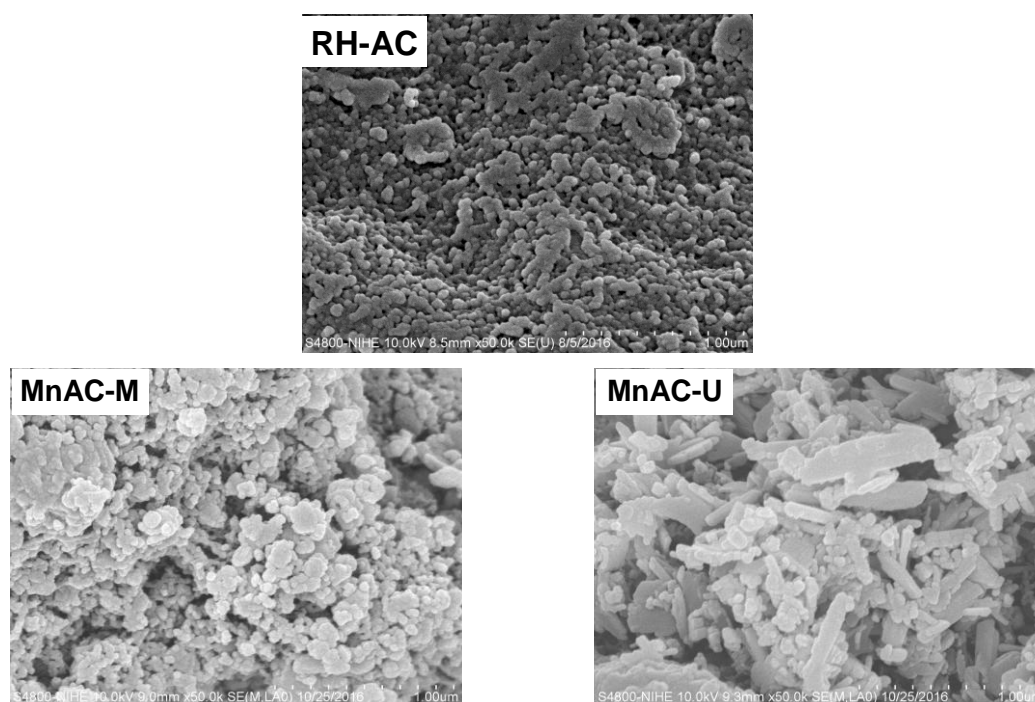


Figure 5. SEM images.

3.1.5. Nitrogen adsorption

The nitrogen adsorption – desorption isotherms of MnAC samples are shown in Fig. 6. All the samples display a typical type I adsorption – desorption isotherm with a small hysteresis loop characteristic of mixed microporous and mesoporous materials [15]. Physical properties of

MnAC samples obtained from N₂ adsorption – desorption are summarized in Table 3. From Table 3, we can see that:

i) As compared to the precursor RH-AC, specific surface area and total pore volume of MnAC samples are much smaller.

ii) Specific surface area and total pore volume of MnAC-M (744 m² g⁻¹ and 0.5065 cm³ g⁻¹) are less than that of MnAC-U (832 m² g⁻¹ and 0.5809 cm³ g⁻¹). The difference in specific surface area is due to the variation in micropore surface area (610 m² g⁻¹ compared to 692 m² g⁻¹). Meanwhile, the difference in pore volume is owing to the co-contribution of micropore volume and mesopore volume (0.3428 and 0.1637 cm³ g⁻¹ compared to 0.3832 and 0.1977 cm³ g⁻¹).

iii) The percentage of mesopore is higher in MnAC-U sample (34.0 % in comparison with 32.3 % of MnAC-M).

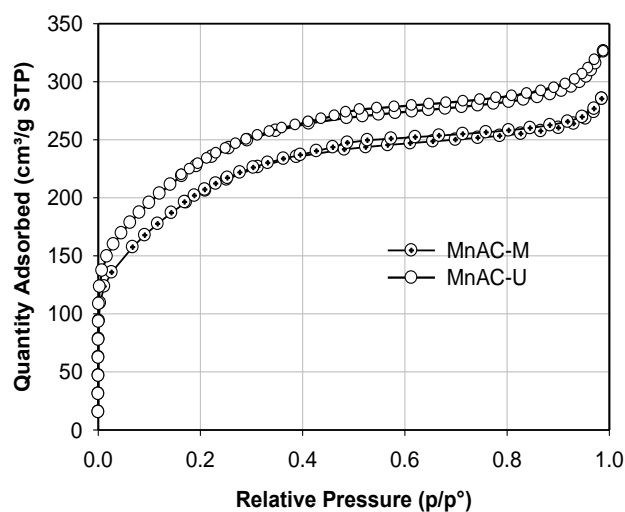


Figure 6. Nitrogen adsorption – desorption isotherms of MnAC samples.

Table 3. Surface area and pore characteristic of MnAC samples.

Sample	S _{BET} m ² g ⁻¹	S _{mic} m ² g ⁻¹	S _{ext} m ² g ⁻¹	V _{mic} cm ³ g ⁻¹	V _{BJH} cm ³ g ⁻¹	V _{tot} cm ³ g ⁻¹	V _{BJH} /V _{tot} %
MnAC-M	744	610	134	0.3428	0.1637	0.5065	32.3
MnAC-U	832	692	140	0.3832	0.1977	0.5809	34.0

S_{BET}: The specific surface area, calculated by applying the BET equation to the adsorption data [16]

S_{mic}, S_{ext} and V_{mic}: The micropore surface area, the external surface area and the micropore volume, evaluated by the t-plot method [17].

V_{BJH}: The mesopore volume, estimated by the Barrett–Joyner–Halenda (BJH) method [18].

V_{tot}: The total pore volume, evaluated by the sum of micropore and mesopore volumes.

The decrease in specific surface area and pore volume is attributed to the presence of MnO₂, which has lesser specific surface area and fewer pores than RH-AC. MnAC-M has higher MnO₂ content than that of MnAC-U, therefore has smaller specific surface area as well as total pore volume.

3.2. Electrochemical properties

3.2.1. Cyclic voltammetry

Cyclic voltammograms recorded between -1.1 and -0.1 V (vs. SCE) in 6 M KOH electrolyte at a scan rate of 5 mV s^{-1} for MnAC-M, MnAC-U, and RH-AC electrodes as well as nickel foam (for comparison) are shown in Fig. 7. No peaks are observed in the case of bare nickel foam, indicating that the nickel foam collector exhibits no electrochemical activity in the investigated potential windows. Rectangular shape is observed for RH-AC electrode indicating EDLC capacitive behavior of the material. For MnAC-M and MnAC-U in the range of -1.1 ~ -0.7 V, the CV curves still keep the ideal rectangular shape similar to RH-AC's which can be ascribed to the contribution of activated carbon. Even though specific surface area of MnACs is much smaller than that of RH-AC (744 and $832 \text{ m}^2 \text{ g}^{-1}$ compared to $2990 \text{ m}^2 \text{ g}^{-1}$), the external surface area of MnACs is slightly different (134 and $140 \text{ m}^2 \text{ g}^{-1}$, in comparison with $243 \text{ m}^2 \text{ g}^{-1}$). During scanning, due to diffusion limitation, the solvated K^+ ions only adsorb/desorb onto mesopore and a minority of micropores, therefore, the decrease in micropores of MnAC did not significantly affect its electrochemical behavior and caused only slightly changed in the shape of CV curves. In the range of -0.7 ~ -0.1 V, MnAC electrodes exhibit an integrated area notably larger than that of RH-AC electrode and display a pair of redox reaction peaks corresponds to the reactions $\text{MnO}_2 + \text{H}_2\text{O} + \text{e}^- \rightleftharpoons \text{MnOOH} + \text{OH}^-$ [19]. Evidently, the integrated area of MnAC electrodes is enhanced by the combination of pseudo-capacitance and electric double layer capacitance. This increase is possibly attributed to the contribution of MnO_2 . MnAC-M has higher MnO_2 content (as pointed out in TGA and TPR- H_2 results), therefore, has a larger integrated area.

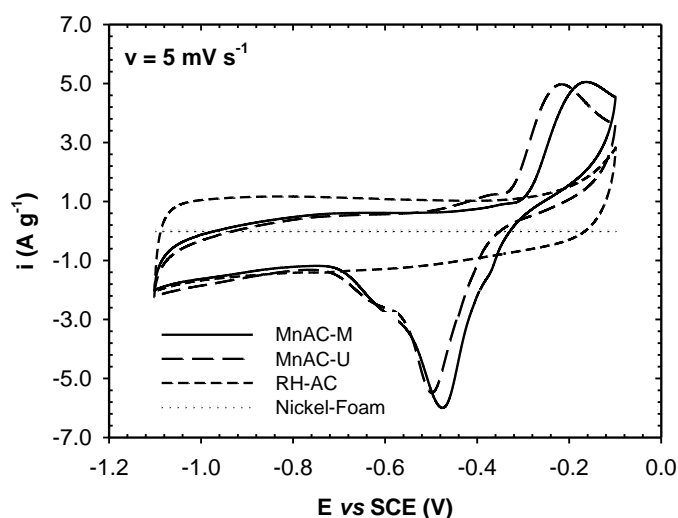


Figure 7. CV of RH-AC and MnAC electrodes in 6M KOH electrolyte at scan rate of 5 mV s^{-1} .

Figure 8 presents the cyclic voltammograms of MnAC-M and MnAC-U electrodes in 6M KOH electrolyte at scan rate from 5 to 50 mV s^{-1} . Peak current increases with the increasing in scan rate. The position of the redox peak shifts slightly at low scan rate and the peak disappeared at scan rate higher than 30 mV s^{-1} , which demonstrates diffusion-controlled kinetic [20].

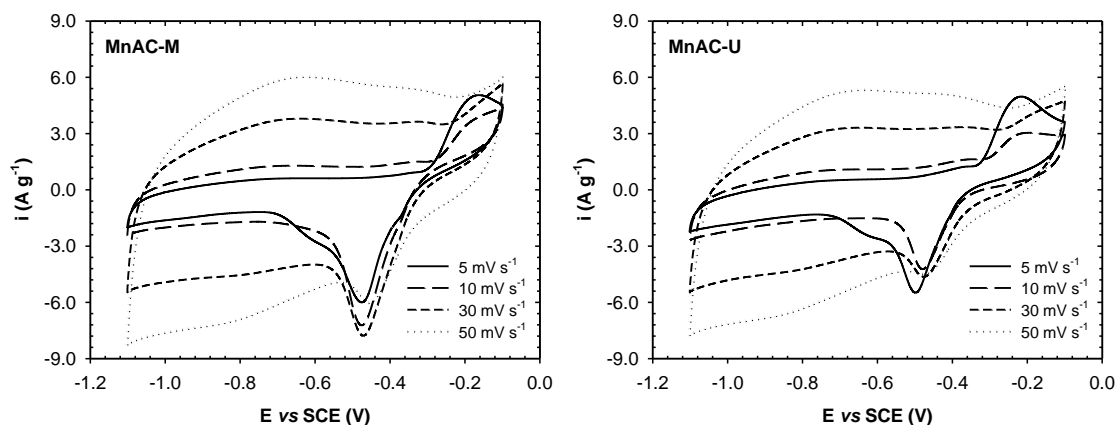


Figure 8. CV curves of MnAC-M and MnAC-U electrodes at different scan rates.

The specific capacitances C (F g^{-1}) were calculated using equation: $C = \frac{\sum |i| \Delta t}{2m \Delta V}$ where $\sum |i| \Delta t$ is the area of the current (A) against time (s), m is the mass (g) of active material in the electrode. The specific capacitances of all samples at different scan rates are summarized in Table 4. It can be seen from Table 4 that:

i) The specific capacitance of all samples decreases with the increasing of scan rate, specific capacitance of MnAC-M and MnAC-U at scan rate of 5 and 50 mV s^{-1} is 338, 320 F g^{-1} and 98, 100 F g^{-1} , respectively. This drop off is due to the decrease in redox reaction rate of MnO_2 and in diffusion rate of K^+ ion at high scan rate.

ii) At low scan rate ($\leq 30 \text{ mV s}^{-1}$), specific capacitance of MnAC-M is higher than that of MnAC-U. This might be due to the high MnO_2 content of MnAC-M sample.

iii) At higher scan rate (50 mV s^{-1}), MnAC-U has better electrochemical behavior, specific capacitance is 100 and 98 F g^{-1} for MnAC-U and MnAC-M, respectively. This result might be explained by the porous structure of MnAC-U. MnAC-U has larger specific surface area and higher mesopore volume (832 $\text{m}^2 \text{ g}^{-1}$ and 0.1977 $\text{cm}^3 \text{ g}^{-1}$) as compared to that of MnAC-M (744 $\text{m}^2 \text{ g}^{-1}$ and 0.1637 $\text{cm}^3 \text{ g}^{-1}$), which is more preferable for K^+ ion to access and resulted in higher specific capacitance.

Table 4. Specific capacitance of the as prepared electrodes.

Sample	C (F g^{-1})			
	5 mV s^{-1}	10 mV s^{-1}	30 mV s^{-1}	50 mV s^{-1}
MnAC-M	338	190	119	98
MnAC-U	320	169	116	100

3.2.2. Charge/discharge test

To further explore the potential application as electrochemical capacitor, charge/discharge experiments were carried out for MnAC-M and MnAC-U electrodes at current density from 0.5 to 3.0 A g⁻¹ over a potential window of -1.1 to -0.1 V.

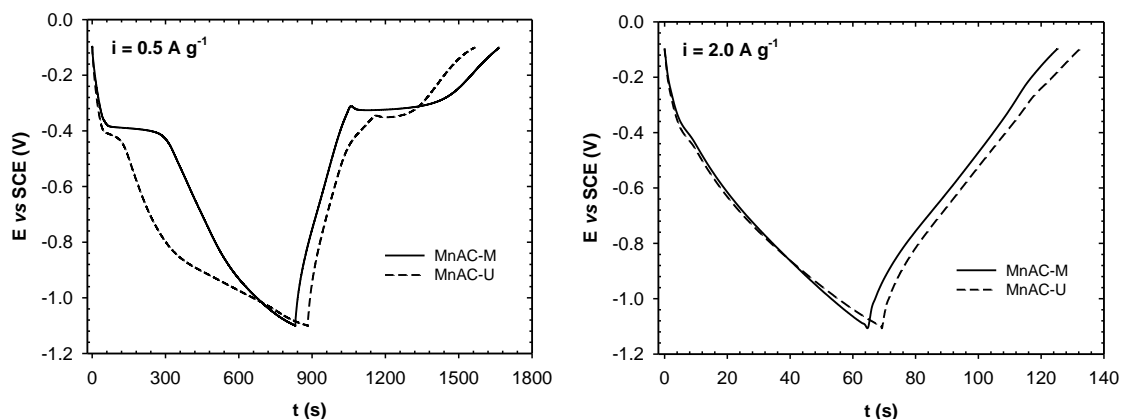


Figure 9. Galvanostatic charge-discharge curves of MnAC-M and MnAC-U at current densities of 0.5 and 2.0 A g⁻¹.

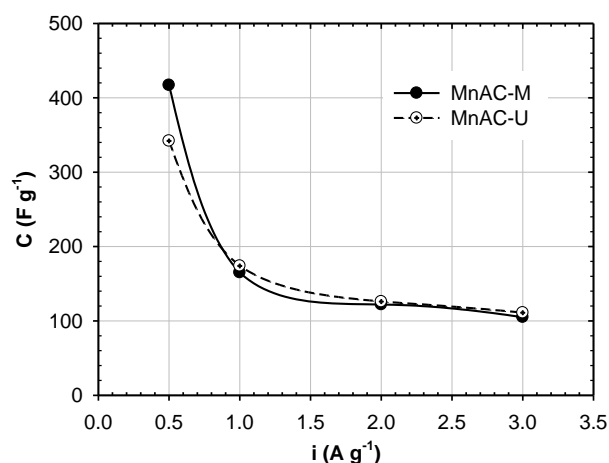


Figure 10. Specific capacitance of MnAC-M and MnAC-U at different current densities.

Figure 9 shows the representative results at current densities 0.5 and 2.0 A g⁻¹. The voltage drops are found to be rather small, indicating the low internal resistance of the electrodes. For current density 0.5 A g⁻¹, the symmetric linear straight lines represent the electric double layer and reversible nature of the electrodes. The short horizontal lines at about -0.2 ~ -0.4 V in the charge/discharge profile are also observed which feature the pseudocapacitive characteristic of the samples [21]. Charge-discharge profiles indicate both the behavior of electric double layer and pseudo-capacitance of the electrodes. For current density 2.0 A g⁻¹, the horizontal lines disappeared, indicating the distribution of EDLC is dominated at high current density, which is agreed well with CV results.

The specific capacitance C (F g⁻¹) is calculated according to the formula:

$$C = \frac{I\Delta t}{m\Delta V}$$

where I is the discharge current (A), Δt is the discharge time (s), m is the mass (g) of the active material, ΔV is the discharge potential range (V). The specific capacitances calculated are illustrated in Fig. 10. The specific capacitances gradually decrease with the increasing of the discharging current density. The specific capacitance of MnAC-M is higher than that of MnAC-U at low current densities and is lower than that of MnAC-U at high current densities. At current density 0.5 A g^{-1} , specific capacitance of MnAC-M and MnAC-U is 417 and 342 F g^{-1} , respectively. However, at current density 3.0 A g^{-1} , the situation is reversed, 111 F g^{-1} for MnAC-U and only 105 F g^{-1} for MnAC-M. This can be explained due to the contribution of MnO_2 is dominated at low current density and the contribution of EDLC is overpowered at high current density as showed in Fig. 9.

4. CONCLUSIONS

The MnAC samples were successfully prepared via magnetic stirring and ultrasonic stirring methods. The resulted samples are amorphous structure with 32~42% MnO_2 loading. The magnetic stirring prepared sample has spherical particles while ultrasonic stirring sample has mixed spherical and rod-like particle. The introducing of manganese oxide resulted in a drop in specific surface area and pore volume compared to activated carbon sample. Electrochemical investigates show that at low scan rate or low current density, MnAC-U have better performance while at high scan rate or high current density, MnAC-M is superior to MnAC-U.

Acknowledgements: This research has received funding from the Vietnam Ministry of Education and Training under grant number B2016-SPH-20.

REFERENCES

1. Wang Y., Song Y., Xia Y. - Electrochemical capacitors: mechanism, materials, systems, characterization and applications, *Chemical Society Reviews* **45** (2016) 5925-5950.
2. Li S.H., Liu Q.H., Qi L., Lu L.H., Wang H.Y. - Progress in research on manganese dioxide electrode materials for electrochemical capacitors, *Chinese Journal of Analytical Chemistry* **40** (3) (2012) 339-346.
3. Lang X., Hirata A., Fujita T., Chen M. - Nanoporous metal/oxide hybrid electrodes for electrochemical supercapacitors, *Nature Nanotechnology* **6** (2011) 232-236.
4. Lee Y. J., Park H. W., Park S., Song I. K. - Electrochemical properties of Mn-doped activated carbon aerogel as electrode material for supercapacitor, *Current Applied Physics* **12** (2012) 233-237.
5. Liu T. T., Shao G. J., Ji M. T., Ma Z. P. - Research progress in nano-structured MnO_2 as electrode materials for supercapacitors, *Asian Journal of Chemistry* **25** (13) (2013) 7065-7070.
6. Xia H., Wang Y., Lin J., Lu L. - Hydrothermal synthesis of MnO_2/CNT nanocomposite with a CNT core/porous MnO_2 sheath hierarchy architecture for supercapacitors, *Nanoscale Research Letters* **7** (2012) 33 (10 pages).

7. Hu J., Sun K., He D., Xu B. - Amorphous Manganese Oxide for Catalytic Aerobic Oxidation of Benzyl Alcohol, *Chin. J. Catal.* **28** (12) (2007) 1025-1027.
8. Figueiredo J. L., Pereira M. F. R., Freitas M. M. A., Orfao J. J. M. - Modification of the surface chemistry of activated carbons, *Carbon* **37** (1999) 1379-1389.
9. Valizadeh S., Younesi H., Bahramifar N. - Highly mesoporous K_2CO_3 and KOH/activated carbon for SDBS removal from water samples: Batch and fixed-bed column adsorption process, *Environmental Nanotechnology, Monitoring & Management* **6** (2016) 1–13.
10. Zhang L. L., Wei T., Wang W., Zhao X. S. - Manganese oxide-carbon composite as supercapacitor electrode materials, *Microporous and Mesoporous Materials* **123** (2009) 260–267.
11. Zolfaghari A., Naderi H. R., Mortaheb H. R. - Carbon black/manganese dioxide composites synthesized by sonochemistry method for electrochemical supercapacitors, *Journal of Electroanalytical Chemistry, Journal of Electroanalytical Chemistry* **697** (2013) 60-67.
12. Bychko I., Kalishyn Y., Strizhak P. - TPR study of core-shell Fe@Fe₃O₄ nanoparticles supported on activated carbon and carbon nanotubes, *Advances in Materials Physics and Chemistry* **2** (2012) 17-22.
13. Ettireddy P. R., Ettireddy N., Mamedov S., Boolchand P., Smirniotis P.G. - Surface characterization studies of TiO₂ supported manganese oxide catalysts for low temperature SCR of NO with NH₃, *Applied Catalysis B: Environmental* **76** (2007) 123-134.
14. Zhou C., Wang H., Peng F., Liang J., Yu H., Yang J. - MnO₂/CNT Supported Pt and PtRu Nanocatalysts for Direct Methanol Fuel Cells, *Langmuir* **25** (13) (2009) 7711-7717.
15. Rouquerol J., Avnir A., Fairbridge C. W., Everest D. H., Haynes J. H., Pernicone N., Ramsay J.D.F., Sing K.S.W., Unger K.K. - Recommendations for the characterization of porous solids, *Pure & Appl. Chem.* **66** (8) (1994) 1739-1994.
16. Brunauer S., Emmett P. H., Teller E. - Adsorption of gases in multimolecular layers, *J. Am. Chem. Soc.* **60** (2) (1938) 309-319.
17. Lippens B. C., de Boer J. H. - Studies on pore systems in catalysts: V. The t method, *Journal of Catalysis* **4** (3) (1965) 319-323.
18. Barrett E. P., Joyner L. G., Halenda P. P. - The determination of pore volume and area distribution in porous substances. I. Computations from nitrogen isotherms, *J. Am. Chem. Soc.* **73** (1951) 373–380.
19. Wang H. Q., Yang G. F., Li Q. Y., Zhong X. X., Wang F. P., Li Z. S., Li Y. H. - Porous nano-MnO₂: large scale synthesis via a facile quick-redox procedure and application in a supercapacitor, *New J. Chem.* **35** (2011) 469-475.
20. Vlad A., Singh N., Rolland J., Melinte S., Ajavan P. M., Gohy J. F. - Hybrid supercapacitor-battery materials for fast electrochemical charge storage, *Scientific Reports* **4** (2014) 4315 (7 pages).
21. Liu M., Kong L., Lu C., Ma X., Li X., Luo Y., Kang L. - Design and synthesis of CoMoO₄-NiMoO₄·xH₂O bundles with improved electrochemical properties for supercapacitors, *J. Mater. Chem. A* **1** (2013) 1380-1387.